Thin photothermal endoscope for biomedical applications

Sreekumar Kaiplavil

Thin photothermal endoscope for biomedical applications

Sreekumar Kaiplavil
Laboratory of Photothermal Science, Pathanamthitta, Kerala 689645, India

Abstract. A thin photothermal (PT) endoscope ($\sim$80 μm) for the noninvasive/minimally invasive hybrid-optical diagnosis of biological specimens is demonstrated. The technique has the unique advantage that the pump laser delivery fiber itself acts as the thermal wave sensor, which is a Bragg grating. It detects only the conductive component of the PT signal, thus enabling an emissivity independent measurement. The device is slidable through a syringe needle and PT analysis of exposed organs with limited accessibility for conventional PT techniques, and constricted regions can be examined noninvasively. For regions buried in thick tissues, a minimally invasive injection mode may be considered. Temperature measurement sensitivity is about 0.03°C. The amplitude and phase channels are sensitive up to about 3 and 10 kHz, respectively. The endoscope has been used for the simultaneous estimation of flow velocity, absorption coefficient, and diffusivity for a phantom-blood flow. The endoscopically estimated values are in agreement with true flow velocities over a range of 1 to 1000 cm^{-1}. The endoscope has been used for the optical biopsy of goat bone marrow. © *2013 Society of Photo-Optical Instrumentation Engineers (SPIE)* [DOI: 10.1117/1.JBO.18.9.097008]

Keywords: photothermal diagnosis; photothermal endoscope; endoscopy; optical biopsy; velocimetry; bone marrow.

Paper 130311R received May 3, 2013; revised manuscript received Jul. 20, 2013; accepted for publication Aug. 21, 2013; published online Sep. 25, 2013.

1 Introduction

Study of photo-induced diffusion waves in matter has paved the way for the development of several revolutionary measurement schemes in basic science, engineering, and medical technology.[1–3] In addition to thermal wave generation, the photothermal (PT) effect and diffusion wave methods take in to account acoustic waves or excited charge carriers or scattered photon fluence rate developed in the medium following periodic optical excitation. The successful applications of this science spread over a wide spectrum that covers measurement of thermophysical parameters of solids and fluids,[4–7] microscopy and tomography,[8–10] wide field thermography,[11,12] noninvasive dental diagnosis,[13] microelectronic metrology,[14] etc. In medicine and biology, both time- and frequency-domain PT analytical methods have been found successful for the noninvasive measurement of peripheral and subsurface tissue parameters.[15–17] Imaging of deep-lying dental caries has been accomplished, with better sensitivity compared to X-rays, with frame synchronized PT wave detection.[18] PT imaging of tumors and infections with the aid of nanocontrast agents[19] and single biomolecule identification[20] and nanocluster-assisted cellular imaging[21] are a few among the recent high potential applications of PT research in medical scenario.

In addition to fundamental studies, during the past three decades considerable attention has been paid in proposing various PT technologies of practical interest for noninvasive clinical procedures such as cytometry, oxygen saturation analysis, depth-resolved skin imaging, monitoring of cell conditions, drug response investigations, etc. Detection of individual cells in blood and lymph flow was demonstrated using a label-free PT pump-probe detection.[22] The concept was further developed for the fast imaging of individual moving cells.[23]

Real-time assessment of circulating clots, dye-cell interaction, and blood flow dynamics is simultaneously carried out using a negative contrast PT-photoacoustic (PA) cytometer.[24] An optical coherence tomography coupled dual wavelength excitation PT method has been proven to acquire a depth resolved picture of oxygen saturation in blood, thus paving a way for the noninvasive pathology related to the early diagnosis of cancer, inflammatory and infectious processes, diabetic retinopathy, choroidal disorders, stroke, and vascular dementia.[25–28] Pulsed PT radiometric depth profiling for the diagnosis of port wine stain[29] and time-domain PA analysis of lymph nodes for melanoma detection[30] are notable for their practical significance in skin cancer screening. PT research in fluid velocimetry has a quite long history of about three decades. Pulsed pump laser induced refractive index modulation accounting the liquid flow velocity with probe beam detection was successful to monitor velocities in the range of 0.2 to 30 mm s^{-1}, in transparent liquids.[31–33] Laser induced thermal lensing and associated probe defocusing[34] and PT deflection with a transient refractive index grating[35] were free from the inherent limitation of laser Doppler velocimetry, which needs scatterers in the fluid. These techniques were equally applicable for laminar and turbulent flow rate measurement. Flow field PA imaging using a detector array and PA Doppler shift measurement are recent promising technologies, which would make the blood flow quantification in microcirculation possible with high sensitivity.[36–38]

In spite of acclaimed scientific advantages, challenges stumbled upon before the adoption of these noninvasive and nonionizing PT methods for realistic clinical trials are many. Relatively low optical absorption in the therapeutic optical window (700 to 1300 nm) and strong absorption of infrared (IR) photons by water molecules in tissues make the available depth information carried by the PT signal at the skin/organ

Address all correspondence to: Sreekumar Kaiplavil, Laboratory of Photothermal Science, Pathanamthitta, Kerala 689645, India. Tel: 1-647-519-7090; E-mail: sreekumarkaiplavil@yahoo.co.in

surface too limited for biologically reliable diagnosis. In other words, conduction-dominated coupling of thermal waves, which are heavily attenuated within the first thermal diffusion length, limits the penetrable depth in tissues to a few hundreds of microns for a practical modulation frequency range (say, 1 to 10 Hz). In the case of pump-probe methods, accuracy of the probe deflection measurement falls down as the tissue thickness increases due to scattering. The fact that emissivity of a surface varies considerably with tissue type and condition, and for the same type from person to person, imposes limitations on the generalized use of PT radiometry methods for biomedical applications.[39] On top of these, most of the techniques are practiced *in vitro* and PT biopsy or cytometry of inner organs, deep-seated tissues, and blood vessels *in vivo* continues to be a challenge.

In this article, we introduce a thin (thickness ∼80 μm) PT endoscope (PTE) that measures the conductive-only component of the PT signal enabling an emissivity independent detection. Both the pump beam delivery and the thermal wave measurement are simultaneously carried out by the same optical fiber sensor. The fiber endoscope is slidable through a syringe needle and can be of any length. These advantages lead to the possibility of noninvasive or minimally invasive PT diagnosis of deep lying anatomical parts, for example, for the screening colon and esophageal cancer, coronary artery blockage imaging, flow analysis of microcirculation, drug response monitoring of internal organs, etc. In Sec. 2, the principle and instrumentation details of the PTE are described. Theory of PT response of a flowing medium is discussed in Sec. 3. Experimental results on the performance, sensitivity, and calibration of the PTE are presented in Sec. 4.1. In addition, the results obtained for a flowing blood phantom are presented. The use of the PTE for bone marrow (BM) biopsy has been demonstrated in Sec. 4.2 as a typical example.

2 Thin PTE

2.1 *Principle*

The heart of the PTE is a fiber Bragg grating (FBG) encrypted on a germanium-doped silica fiber of about 80-μm thick.[40,41] The well-known dependence of Bragg wavelength (λ_B) on the grating temperature, which is about 10 pm K^{-1}, is the mechanism used for sensing the laser-induced thermal signal in the sample. The grating offers excellent transmission for all wavelengths except for a sharp notch at λ_B. An FBG with Bragg wavelength in the C-band (1530 to 1565 nm) is, therefore, an efficient carrier of visible or near IR pump. Figure 1 shows the instrumental configuration of the device. A thermally
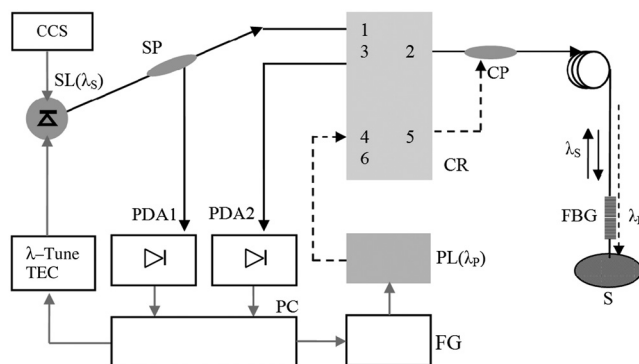
tunable C-band distributed feedback (DFB) diode laser [sensing laser (SL)], whose spectrum contains the Bragg wavelength, is coupled to the FBG through ports 1 and 2 of a fiber-optic circulator (CR). The reflected signal (at port 3) is detected using a C-band photodiode (G17BOC-07, Perkin Elmer, Massachusetts) and a transimpedance amplifier (PDA2) wired around an OPA657 operational amplifier. The DFB temperature is set using a thermoelectric cooler, which is under the control of a computer (PC). A constant current source (CCS) powers the DFB laser. Over a reasonable spectral band (∼10 nm, for common modules), the DFB wavelength is proportional to its temperature. The FBG wavelength has been selected such that at 37°C (normal human body temperature) it corresponds to the central portion of the available DFB spectral band. The pump laser (589-nm diode) is coupled to the endoscope fiber using a 2 × 1 coupler, through ports 4 and 5 of the CR. We consider a simplified geometry of the FBG reflection spectrum with the overlap of the probe laser line as shown in Fig. 2. Here λ_L and λ_U are, respectively, the lower and upper wavelength limits of the linear portion of the reflectance spectrum, and λ_C is the operating point. An arbitrary temperature change causes a shift in the Bragg wavelength through D such that the reflected intensity changes from I_C to I_D. From the results of trigonometry, it can be shown that

$$\frac{I_C}{I_D} = \frac{\lambda_C - \lambda_L}{\lambda_C - (\lambda_L + D)}. \tag{1}$$

The Bragg wavelength being dependent on the ambient (specimen) temperature, an initial calibration is essential before starting the measurement to fix the operating point. For this, the sensor tip is placed in thermal contact with the specimen keeping the pump laser OFF. The SL temperature and, consequently, its wavelength are swept over a band which covers the full spectral width anticipated for the FBG reflection spectrum, with a reasonable margin on both edges. Reflected light intensity is recorded as a function of TEC control signal to which both the laser temperature and wavelength hold a liner relationship. Knowing the control signal values corresponding to wavelengths λ_L and λ_U (or λ_B), an optimum operating point may be identified at the arithmetic mean value for these boundaries. The entire process is completed in a couple of minutes under computer control in LABVIEW environment. Once the operating point is identified, the DFB temperature (and wavelength) is fixed there and any subsequent change in the reflected light intensity will be proportional to the change in temperature of the grating.
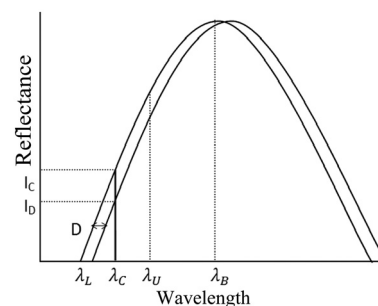

Fig. 1 Schematic of the thin photothermal (PT) endoscope.

Fig. 2 Geometry of the fiber Bragg grating (FBG) reflection spectrum with the overlap of probe laser line.

2.2 Implementation of the PTE

The Bragg wavelength of the grating we considered was 1535.934 nm with the center of rising edge of reflection located at 1535.881 nm, at 25.00°C. The sensing terminal of the fiber was cut in such a way that ~90% (verified through reflectance measurement) of the grating (~0.5-mm long) remained on the fiber. The half power spectral width was about 200 pm with a peak reflectance of about 40%. As the SL, we used a Lucent E2505-H52 DFB diode module that has, at 25°C, 1535.820 nm emission, 20-pm half power spectral width and 2 mW (max) power at the fiber output. It has a built-in TEC for wavelength tuning. Not only the DFB wavelength but also the output power is a function of temperature (power decreases with temperature). For normalizing the sweep data against this dependence, the DFB output is sampled using a splitter (SP) and a photodiode (PDA1). The observed values of λ_S were 1532.884 and 1537.375 nm for TEC temperatures 0°C and 30°C, respectively. This sweep range (4.491 nm) corresponds to a possible temperature measurement range of about 0°C to 450°C with the FBG, which is too large for dealing with realistic PT signal levels in biological specimens. Output current noise density of the CCS is about 1 nA/$\sqrt{\text{Hz}}$ and stability is about 30 ppm/°C. The stability of DFB temperature set point is better than 0.005°C. The grating is inserted through a syringe with needle [Fig. 3(a)]. A manual sliding mechanism facilitates smooth glide of the fiber through the needle. The key advantage of this approach is that a minimally invasive injection mode may be followed for probing regions buried in thick tissues. The needle may be inserted with the fiber tip lifted up to a safe position within the needle and sensor-specimen thermal contact may be established by sliding it down until the needle tip reaches the location of interest. Furthermore, exposed organs with little accessibility for conventional PT analysis (esophagus, colon, auditory canal, nostril, etc.) and constricted regions can be examined noninvasively if the needle is made sufficiently long and properly bent. Figure 3(b) is the photograph of the PTE sliding through a typical 2-ml syringe.

3 Theory of PT Signal Generation in a Flowing Liquid and PT Endoscopic Blood Flow Cytometry

Various theoretical models have been proposed to describe the PT effects in streaming as well as static fluids with gas-microphone,[42] optical beam deflection,[43] and radiometric detection techniques.[44] Owing to the lower content of static PT signal (dc component), pulsed excitation has widely been considered for biologically important diagnostic applications in which the maximum permissible exposure limits the deliverable laser
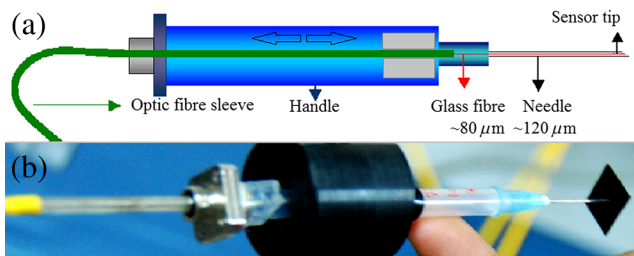
energy and the available signal quality.[45] In the following treatment, we make use of the pulsed PT excitation of a flowing medium (general case) and a time-domain analysis of the resulting thermal transient detected by the endoscopic tip. Figure 4 shows the endoscope inserted into a blood vessel in which the flow is along the x-direction and the endoscopic axis is normal to the flow velocity. It is realistic to assume that the heat transfer mechanism within the sample is conduction because radiative coupling is highly suppressed due to strong IR absorption by water present in blood. The heat diffusion within the sample obeys the equation:

$$\frac{\partial T(r,t)}{\partial t} = \alpha \nabla^2 T(r,t) - v\frac{\partial T(r,t)}{\partial x} + \frac{\alpha}{k}Q(r,t). \quad (2)$$

Here, $T(r,t)$ is the temperature rise due to optical absorption, v is the flow velocity along the x-direction and α and k are, respectively, the thermal diffusivity and conductivity of the medium. $Q(r,t)$ is the heat produced per unit volume of the medium and r and t are, respectively, the position and time at which measurement is carried out. We assume a situation in which the medium is thermally thick and the optical absorption length (μ_a) in the sample is much larger than the thermal diffusion length (μ). Furthermore, the scattering coefficient is small compared to the absorption coefficient at the pump wavelength used. The optical energy is thus completely dissipated in the medium due to absorption within a spatial domain, which is larger than a diffusion length. In this conduction-dominated thermal coupling scheme, the endoscopic tip measures the depth integrated thermal signal generated within approximately one diffusion length in the medium. With these assumptions, one can presume the medium to be a weak absorber for which the heat produced per unit volume is given by

$$Q(r,t) = \begin{cases} \frac{2\mu_a E}{\pi a^2 \tau} e^{-\frac{2r^2}{a^2}} & \text{for } 0 \leq t \leq \tau, \\ 0 & \text{for } t \geq \tau \end{cases} \quad (3)$$

where E is the energy per pulse of the pump and τ is the pulse width. The pump laser beam is assumed to have a Gaussian profile with $1/e^2$ radius a. For small values of numerical aperture, the pump radius may be approximated to the endoscopic fiber radius provided the thermal diffusion length is small (say, a few tens of microns). For a general solution to Eq. (2), the law of conservation of energy should be satisfied as an essential criterion. This means that there should not occur any energy conversion process like phase transition, radiative recombination processes, PA signal generation, etc., other than nonradiative (thermal) relaxation of the medium. For minimizing PA effects, the use of appropriate pulse duration should be considered such
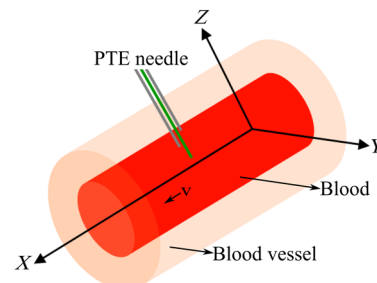

Fig. 3 (a) Architecture of the photothermal endoscope (PTE). The lowest inner needle diameter used was 120 µm. (b) Photograph of the laboratory prototype.

Fig. 4 The PTE needle injected into a blood vessel.

that stress and thermal confinement conditions are not met.[46] Energy loss via radiative fluorescence emission occurs in most biological specimens. However, one has to consider an excitation wavelength for which the radiative energy conversion efficiency is negligibly small compared to the thermal conversion efficiency for these samples.[47] A two-dimensional solution to Eq. (2) with an axial (x-direction) and radial (y-direction) heat diffusion leads to the resulting temperature distribution[32,48]

$$T(x,y,t) =$$
$$\frac{2\mu_a \alpha E}{\pi k \tau} \int_0^\tau \left[\frac{\exp\{[-2[x-v(t-s)]^2 + y^2]/[8\alpha(t-s)+a^2]\}}{8\alpha(t-s)+a^2} \right] ds$$
$$\text{for } t > \tau.$$
$$(4)$$

If we assume that the pulse repetition frequency (PRF) is large enough to make the diffusion length much smaller than the radial extension of the thermal wave field and measurement is done at the center of the fiber face, then $y = 0$ and Eq. (4) assumes a one-dimensional form. In this case, $T(x,t)$ will be the thermal wave distribution in the fluid layer, which is in contact with (or within the close vicinity of) the endoscopic tip.

Equation (4) does not have an analytical solution, and hence it has to be solved numerically. This numerical integration has been carried out using the MATLAB function "quadv," for $t > \tau$. In Fig. 5, simulated PT transient response of blood at 589 nm for a band of velocity values has been depicted. Assumed thermophysical parameters of human blood are $\mu_a = 80$ cm^{-1}, $k = 0.5$ W m^{-1} K^{-1}, specific heat capacity at constant pressure $C_p = 3500$ J kg^{-1} K^{-1} and density $\rho = 1100$ kg m^{-3}.[49] These values lead to a diffusivity of about 1.3×10^{-7} m^2 s^{-1} according to the relation $\alpha = k/\rho C_p$, $E = 5 \times 10^{-6}$ J, and $\tau = 1 \times 10^{-4}$ s. PRF is 20 Hz for which μ in blood is about 20 μm. Assuming that the PTE measures integrated thermal wave contribution over one diffusion length, the integration was carried for an axial distance $x = \mu$. In the above treatment, we believed that excitation energy was low enough to forbid the occurrence of PT saturation.[50] In Fig. 6, the transient response for a set of diffusivity values is plotted. The transient amplitude has strong dependence on the flow velocity and it decreases as
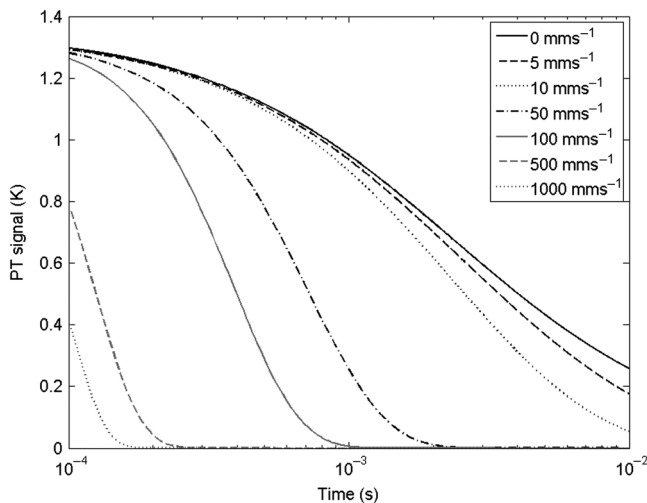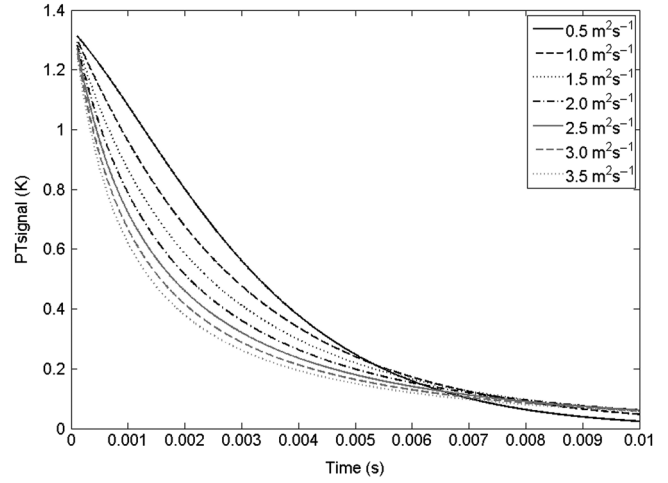

Fig. 6 Simulated PT transient response of static blood, for excitation at 589 nm, for the diffusivity range of 0.5×10^{-7} to 3.5×10^{-7} m^2 s^{-1}.

the speed increases. The velocity characterizes the rate of decay, too. From Fig. 6, it is evident that the early thermal transient signal is almost independent of diffusivity variation over a broad range. This is a consequence of the fact that immediately after the laser goes off, for an interval which is much shorter than the diffusion time ($t_d = a^2/4\alpha$), diffusive loss is negligible and the amplitude is chiefly controlled by the absorption and forced convection (flow rate). For late transient, the curve shape depends not only on velocity but also on diffusivity. For a known value of pump beam radius, simultaneous measurement of absorption coefficient, diffusivity, and flow velocity is possible through multiparameter fitting of experimental data with the theory [Eq. (4)] with ensured uniqueness.[51] To strengthen the inimitability of the fitting process, a frequency-domain approach, too, is considered for the simultaneous evaluation of diffusivity and absorption coefficient. For a thermally thick sample, if $1/\mu_a > \mu$, the tangent of the PT signal phase (φ) depends only on μ_a and μ:[52]

$$\tan \varphi = \frac{\text{Im}(T)}{\text{Re}(T)} = -\left(1 + \frac{2}{\mu_a \mu}\right) = -\left(1 + \frac{2}{\mu_a}\sqrt{\frac{\pi f}{\alpha}}\right). \quad (5)$$

Here, f is the modulation frequency. In contrary to the large variation of μ_a with the degree of blood oxygenation, the spread of diffusivity values is small. Moreover, it has been reported that the diffusivity of blood does not vary much from person to person and it is insensitive to flow dynamics as well.[53] Therefore, one can assume a literature value for diffusivity as a seed parameter for fitting the frequency swept data with Eq. (5) for the simultaneous estimation of μ_a and α. A nonlinear least square fitting algorithm cancels the instrumental phase offset through self calibration.

4 Experiment and Results

4.1 Frequency Response and Sensitivity of the PTE

The frequency response of the PTE was studied and the results are plotted in Fig. 7. For this, the tip was kept in contact with Indian ink taken in a $5 \times 5 \times 5$ cm^3 dish. Pumping was done at low power ($\sim$5 mW, 589 nm) to avoid convection currents and frequency-swept (sinusoidal) data were collected over the range from 1 Hz to 10 kHz using a digital lock-in amplifier. The
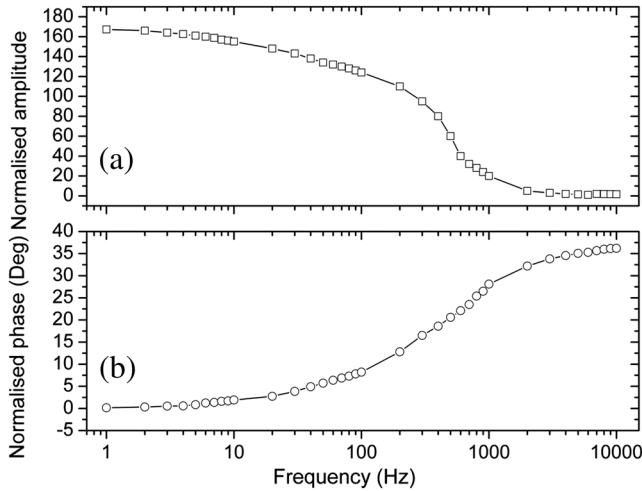

Fig. 5 Simulated PT transient response of blood, for excitation at 589 nm, for the flow velocity ranging from 0 to 1000 mm s^{-1}.

Fig. 7 Frequency response of the PTE: (a) amplitude and (b) phase. An offset correction has been applied to the phase to read 0 deg at 1 Hz.

theoretical PT response of a semi-infinite opaque material was considered for normalizing the experimental data. For this, amplitude ratio and phase difference were estimated for the respective experimental and theoretical values. The -3 dB amplitude response is ~ 200 Hz. The amplitude is detectable up to ~ 3 kHz and the phase to ~ 10 kHz. Because of two reasons the sensitivity of the amplitude channel becomes greatly reduced at higher frequencies (say, >3 kHz): (1) the strong attenuation of PT signals and (2) as the thermal diffusion length decreases, the number of grating lines that are thermally excited is decreased; this, in turn, reduces the intensity of reflected laser intensity. On using higher pump powers, the frequency response was observed to be slightly broadened provided the irradiation time is small enough to forbid the generation of thermal currents in the ink. The frequency roll-off is, however, not a drawback as most theoretical models (with fitting algorithm) for PT measurements are self-calibrating against instrumental transfer function. We measured the sensitivity of the endoscope by attaching it to a small TEC heating element, which was under the control of a temperature controller (0.005°C resolution). Element temperature was changed from 36°C to 38°C with an interval of 0.01°C, and the PTE output was recorded. For 10 trials, the uncertainty in PTE-measured temperature was found to be ~ 0.03°C.

4.2 Measurement of Flow Velocity, Absorption Coefficient, and Diffusivity

Experimental arrangement for blood velocimetry consists of a 250-ml syringe pump, which controls the flow through a 2-m long tygon tube of inner and outer radii 2.5 and 3.5 mm, respectively. The true flow velocity is calculated in terms of the volume of liquid flown, area of the tube, and time of flow (dispensed volume = area × velocity × time). The blood-mimicking phantom was red fountain pen ink solution containing distilled water and ink in the ratio 3 : 1. Absorption coefficient for this ratio at 589 nm was found (using Ocean Optics PC-1000 spectrophotometer and Beer–Lambert's law) to be 112 ($\pm 5\%$) cm^{-1}, which is comparable with that of whole blood. If one assumes that the diffusivity values of the phantom and water are almost equal (1.4×10^{-3} cm^2 s^{-1}), then at 22.5 Hz, the diffusion length becomes half of the absorption depth.

So, a frequency band above this value could be used for generating sweep-data for fitting with the theory (Eq. 5), which is valid only if $1/\mu_a > \mu$ in the thermally thick regime. The endoscope was injected into the tube, which contained a static column of ink, making an angle of ~ 45 deg with the tube axis. The tip was positioned to coincide with the diametric center of the tube. Sinusoidal excitation (40 to 400 Hz) at a peak power of 5 mW (589 nm) and lock-in detection were employed to record in-phase and quadrature signals. Figure 8 shows the tan φ versus frequency data and the theoretical fit. The best fit values are $\alpha = 1.61 \times 10^{-3}$ ($\pm 4\%$) cm^2 s^{-1} and $\mu_a = 98.52$ ($\pm 3\%$) cm^{-1}. The fitted and the spectroscopically measured values of μ_a are in reasonable agreement.

For transient analysis, 1-ms pulse of amplitude 10 mW with a PRF of 20 Hz was used as the pump. Transient signal at the endoscope output was digitized using a 12-bit data acquisition card of 1-MHz bandwidth. The digitizer was enabled by the falling edge of the laser pulse since the theory [Eq. (4)] was developed for the PT decay. For averaging, 30 transients were recorded. For different flow velocities over the range of 1 to 10^4 mm s^{-1}, transients were analyzed. Figure 9 shows the transient recorded at 50 mm s^{-1} and the corresponding best fit [Eq. (4)]. For initializing iterations, seed values assumed for μ_a and α were 112 cm^{-1} and 1.4×10^{-3} cm^2 s^{-1}, respectively. An instrumental constant, which appears as a signal-scaling factor during the fitting process, was also included as a parameter. The best fit values are $v = 57.3$ ($\pm 4\%$) mm s^{-1}, $\alpha = 1.24 \times 10^{-3}$ ($\pm 5\%$) cm^2 s^{-1}, and $\mu_a = 121$ ($\pm 4\%$) cm^{-1}. These values were obtained by putting a slightly larger value (65 μm) for the beam radius instead of the exact fiber radius (40 μm), in the computation of Eq. (4). It is meaningful to assume in this context that the diverging nature of the pump beam (due to fiber delivery) and possible scattering make the radial dimension of the beam within the solution larger than the true fiber radius. So, the pump radius was considered as an optimization parameter for the best fitting results. Despite the fact that there is a notable difference in the values of α and μ_a estimated through the uncorrelated frequency-domain and time-domain analyses (22% for α and 18% for μ_a), the
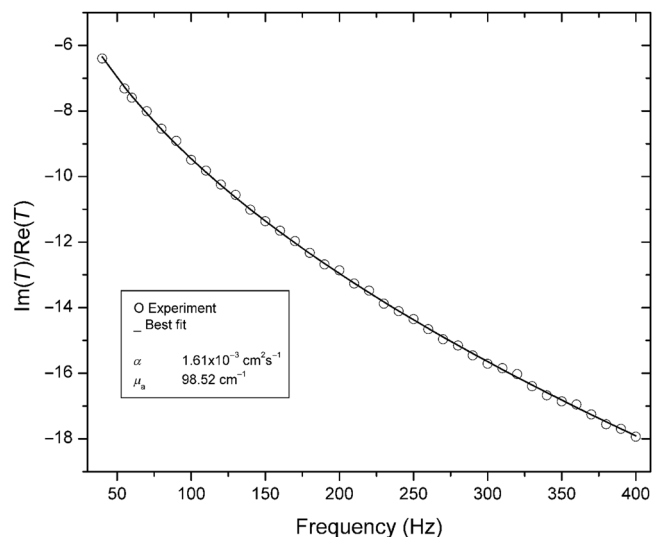

Fig. 8 Frequency-swept $\mathrm{Im}(T)/\mathrm{Re}(T)$ response (open circles) of static ink solution excited with 589-nm diode laser and the best theoretical fit (dash).
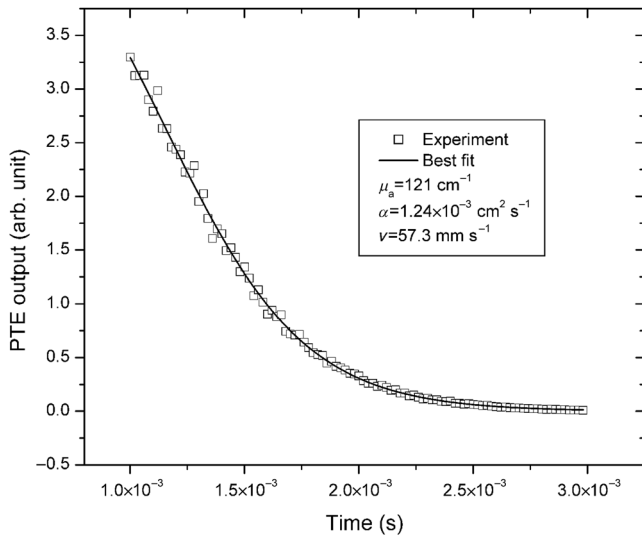
Fig. 9 PTE output recorded for flowing ink (open squares) and the best theoretical fit (dash). Pump wavelength is 589 nm.

benefit of having them together is the ensured fitting uniqueness for the latter, which has three parameters to be evaluated.

In Fig. 10, diffusivity and absorption coefficients of the flowing ink solution, measured from the transient response recorded by the endoscope, are plotted as a function of true flow velocity. For low flow velocities, the measured diffusivity is almost equal to that of the static liquid (1.24×10^{-3} cm^2 s^{-1}) with an error band of $\sim \pm 5\%$ [Fig. 10(a)]. For higher speeds, say above 10^3 mm s^{-1}, there is a fall in the estimated diffusivity values and the error band increases considerably. This is because the rate of forced convection over-rides the influence of diffusion on the signal at higher speeds. As the combined effect of this faster heat removal from the point of excitation and inappreciable thermal diffusion (within the acquisition interval), the signal level comes down with increasing transient slope at higher speeds. Consequently, the uncertainty goes up. In the case of absorption coefficient, the PTE measured value is almost insensitive to the flow velocity [Fig. 10(b)]. However, the error band is found to be widening with velocity. This is a consequence of the rapid fall in the signal level at higher speeds.
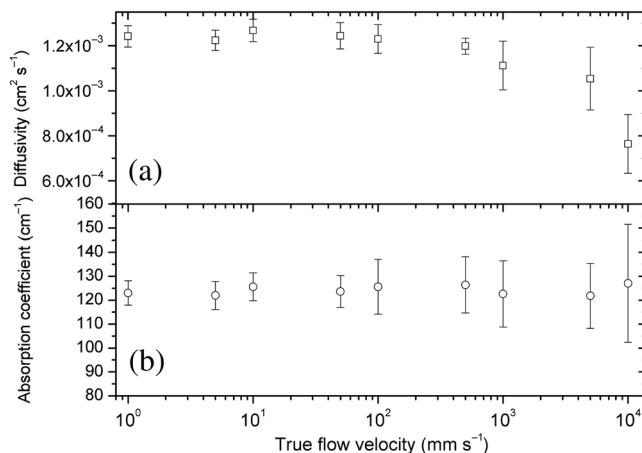
In Fig. 11, the PTE measured flow velocity is plotted against the true velocity. A linear relationship is maintained at higher velocities coarsely >10 mm s^{-1}. At low speeds, the velocity is overestimated with increasing uncertainty as the flow slows down. The cause of this can be attributed to the boundary (sensor liquid) heat losses due to the convection currents setup in the medium, the relative magnitude of this quantity with the flow speed being a key parameter. The characteristic times for building up convective effects for various sample/heating configurations are well documented in the literature.[54] At low flow velocities, the forced removal of energy is a slow process and the characteristic time for this process is comparable with the time for establishing free convection for the endoscope-liquid configuration, which is not perfectly adiabatic. This means, for low speeds, the rate of energy removal, which is controlled by the convective flow, as well as the streaming liquid molecules appears overestimated, because their magnitudes are comparable. Therefore, there is an apparent increase in the estimated flow velocity.

4.3 BM Biopsy

The BM examination refers to the pathologic analysis of samples of BM obtained by BM biopsy and aspiration.[55] This analysis is recommended for the diagnosis of a number of conditions such as unexplained low red blood cell count (anemia), low white cell count (leucopenia), low platelet count (thrombocytopenia), tumors of the lymphoid tissues (lymphoma), etc. Also, monitoring and evaluation of leukemias, iron level problems, unexplained spleen enlargement (splenomegaly), etc., are usually carried out through marrow biopsy.[56] Because of the rapid reproduction of BM cells and the short life span and minimal storage in the BM of circulating cells, BM cells and their precursors are particularly vulnerable to physiologic changes that can affect cell production. Optical and structural properties of BM cells have been found to be indicators of several physiological disorders. For example, optical absorption coefficient is identified as a potential marker to discriminate normal lymphocytes form lymphoblast of acute lymphoblastic leukaemia.[57] BM micrometastases, which elude radiographic detection, have been identified using luminescence imaging.[58]

Fig. 10 Dependence of endoscopically measured diffusivity (a) and absorption coefficient (b) of the flowing ink solution on the true flow velocity.
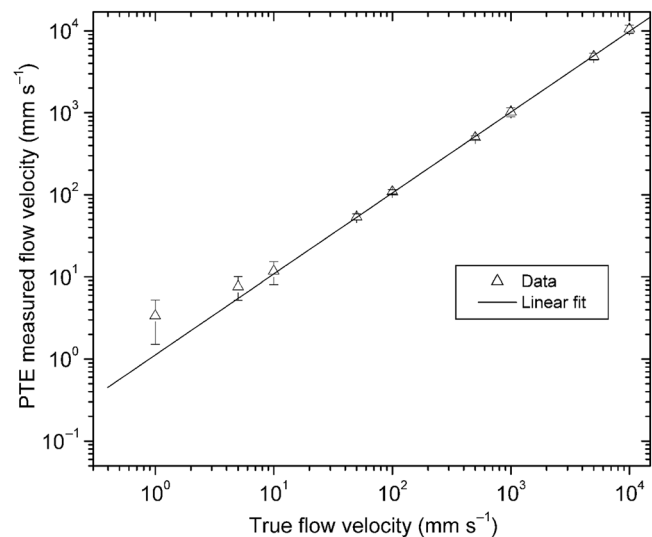

Fig. 11 Endoscopically measured flow velocity versus true velocity for the ink solution.
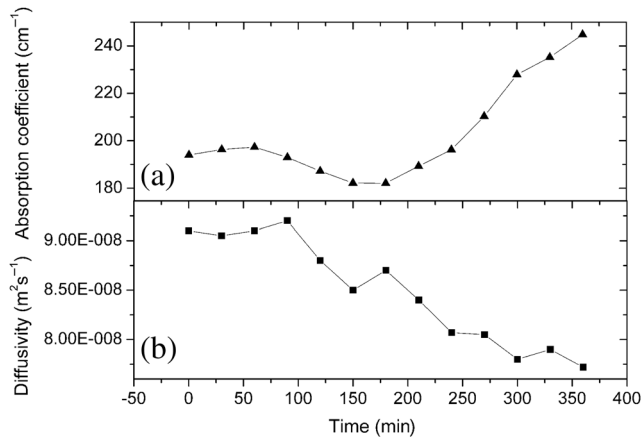
Fig. 12 Variation of (a) absorption coefficient and (b) thermal diffusivity of goat shoulder marrow with time, estimated using PTE. The bone had ~2-cm thick meat over it.

Sickle-cell disease whose major cause is the low oxygenation in marrow leading to deoxyhemoglobin dominance is detectable through absorption spectrometry.[59] In another interesting report, IR spectroscopy has been successfully used to monitor oxygen saturation changes during orthostatic variations imposed by body tilt.[60] Fluorescent microscopy with the use of Truant's auramine–rhodamine staining of BM aspirates has been found to be a sensitive and rapid technique for determining the presence of mycobacteria in BM specimens from patients with HIV infection.[61]

For BM biopsy, usually an aspiration needle is used to collect the marrow sample and pathological analysis is done *in vitro*. The challenge behind *in vivo* biophotonic BM biopsy can be lucratively accomplished using the PTE, the markers being absorption coefficient and diffusivity. We made an attempt to demonstrate BM biopsy in a goat shoulder purchased from a butcher shop. The shoulder was ~10-cm long with a 2-cm-thick meat over layer. The sample was cut at both ends so that the marrow cross-sections were exposed to the atmosphere. The animal had been sacrificed ~2 h before the experiment commenced. An aspiration needle of ~400-μm inner radius was inserted into the bone through the meat. The PTE needle (~300-μm outer radius) that contained the endoscope fiber was slid through the aspiration needle. The sensor tip was properly positioned to ensure physical contact with marrow by monitoring the output signal level. PT transients were recorded as a function of time with an interval of 30 min for 6 h, and α and μ_a were estimated. Excitation wavelength was 589 nm. As shown in Fig. 12(a), the absorption coefficient has a smooth decrease first and then goes on increasing. The increasing value of μ_a may be attributed to oxy- to deoxyhemoglobin conversion. The estimated α has a little unsteady but decreasing trend with time. However, many biochemical processes are responsible for the initial lowering of μ_a as well as the unsteady fall in α with time. No effort has been made to understand the full mechanism behind these trends as it is beyond the scope of this article.

5 Discussion

In this article, we propose a thin PTE having an 80-μm-thick Bragg grating sensing tip, which acts as the pump carrier as well. The device measures conductively coupled thermal waves and its response is insensitive to the emissivity of the sample/organ. The endoscope can be of any length to facilitate

PT diagnosis or biopsy of deep-lying as well as peripheral organs *in vivo*. The time-domain transient analysis considered for the simultaneous determination of optical absorption coefficient, thermal diffusivity, and flow velocity is fast enough to make it a potential device for clinical diagnostics applications. The fiber sensor being slidable through a syringe needle, biopsy of regions concealed within hard tissues or thick soft tissue layers is possible. The endoscope is a sterilizable one. The measured sensitivity (~0.03°C) and bandwidth (~3 and 10 kHz for amplitude and phase, respectively) are reasonable to cope with most of the PT measurements. The theoretical treatment considered here assumes an energy conservation criteria for which there should not occur any energy conversion process like phase transition, radiative recombination, PA signal generation, etc., other than nonradiative de-excitation leading to thermal wave generation. Among these, PA signal generation and radiative processes resulting in fluorescence emission need special attention even at low powers. If the stress and thermal confinement conditions are met, the tissue will act as a source of PA signals with a possible frequency bandwidth of ~1/pulse-width. An FBG is sensitive to strain also and the PA waves getting coupled to it will convolute with the thermal response. For a pulse duration, which is longer than the thermal diffusion time, PA conversion efficiency will be negligibly small. In our experiment, a pulse width, which is close to the thermal relaxation time (3.6 ms for blood) was considered. We inserted a fourth order low-pass filter of 330 Hz cut-off frequency in the output signal channel. An unfavorable consequence of this filtering is attenuation for the early transient, which is likely to introduce error in the measurement of absorption coefficient and flow velocity. To have a better look into this issue, we made measurements with and without the filter and the estimated values of α, μ_a, and v did not differ >2%. Furthermore, we repeated the measurement with 1-ms pulse and 1-kHz filter. Here also, the difference was <2%. The problem of radiative energy conversion can be resolved through selecting an optimal excitation wavelength.[47,62] For most of the tissues, the fluorescence conversion efficiency rapidly falls >500 nm. The wavelength used in this work (589 nm) is thus appropriate in this regard. Moreover, at this wavelength, absorption coefficients of oxy- and deoxyhemoglobins differ by an order of 10 leading to the possibility of oxygen saturation studies and related diagnostic procedures.

Spectroscopically and endoscopically measured values of absorption coefficient of red ink solution are found to differ by about 7%. A major reason for this difference is the bandwidth limitation of the PTE which attenuates a portion of the very early thermal transient containing vital information about the total absorbed energy. The best transient fit was observed when the pump radius was slightly increased beyond the fiber radius. This is a consequence of the diverging nature of the beam as well as scattering occurring in the liquid, which is not accounted for in the theoretical model. For low flow velocities, <10^3 mm s^{-1}, the estimated diffusivity values are the same as that of static liquid. For higher speeds, the combined effect of faster heat removal from the point of excitation and insignificant thermal diffusion within the acquisition interval lead to an underestimated diffusion coefficient. In velocimetry, the system being not perfectly adiabatic, notable discrepancies occur for low velocities leading to overestimation with increasing uncertainty with decreasing velocity. The cause of this can be attributed to the boundary heat losses due to the convection

currents. At low flow velocities, the forced removal of energy is a slow process and the characteristic time for this process is comparable with the time for establishing free convection for the endoscope-liquid configuration, which is not perfectly adiabatic. Since the current method assumes one-dimensional heat diffusion in a semi-infinite medium, suitable sample boundary conditions should be strictly satisfied for reliable results. For example, in blood flow velocimetry, the vessel wall should be several diffusion lengths (say, 5 to 10) away from the endoscopic tip so that edge effect is negligible.[63] This imposes restrictions on the vessel size. So at 20 Hz, the vessel inner diameter should be $>200 \ \mu m$ to forbid thermal wave interference effects. The thermal thickness condition for reliable frequency-swept analysis, $1/\mu_a > \mu$, also limits the minimum vessel dimension according to the lowest frequency considered. For improved performance, a rigorous theoretical model for three-dimensional heat diffusion around the PTE tip incorporating scattering effects, pump beam divergence, effect of convection, PA energy conversion, etc., with the current considerations should be formulated. Another key parameter is the angle between the flow direction and endoscopic axis. We made measurements in a tube of 1-cm diameter for angles of 45 deg downstream, 45 deg upstream, and 90 deg with stream, the tip being at the diametric center always. The observed variation in α was about 3% and that in μ_a was negligible. A large diameter tube was considered for minimizing viscous gradient in the close vicinity of the PTE by maintaining equivelocity liquid layers in that region.[64] As an issue that needs special attention, we have considered the influence of the metallic needle on thermal diffusion in the glass fiber sensing tip. Thermal diffusion length in glass at 20 Hz is about 80 μm.[65] The grating is distributed over a length of ~500 μm. We measured the amplitude and phase of PT signal generated in black ink as a function of the fiber length outside the needle (*l*). It was found that for *l* > 40 μm (approximately), the amplitude and phase were independent of *l*. The usefulness of the PTE for optical BM biopsy has been demonstrated, which is not practicable with conventional PT or PA techniques especially when there is thick over layer of soft tissue. Identifying the mechanism behind the observed variation of μ_a and α with time does not fall within the scope of this work. However, monitoring these parameters for deep-seated and inaccessible organs is of considerable medical significance.

Acknowledgments

References

1. A. Rosencwaig, *Photoacoustics and Photoacoustic Spectroscopy*, John Wiley, New Jersey (1980).
2. D. P. Almond and P. M. Patel, *Photothermal Science and Techniques*, Chapman and Hall, London (1996).
3. A. Mandelis, "Diffusion waves and their uses," *Phys. Today* **53**(8), 29–34 (2000).
4. A. Mendioroz et al., "Thermal diffusivity measurements of thin plates and filaments using lock-in thermography," *Rev. Sci. Instrum.* **80**(7), 074904 (2009).
5. J. A. Baldreas-Lopez and A. Mandelis, "Self-consistent photothermal techniques: application for measuring thermal diffusivity in vegetable oils," *Rev. Sci. Instrum.* **74**(1), 700–702 (2003).
6. I. A. Esquef et al., "Photothermal gas analyzer for simultaneous measurements of thermal diffusivity and thermal effusivity," *Anal. Chem.* **78**(14), 5218–5221 (2006).
7. M. A. Owens, C. C. Davis, and R. R. Dickerson, "A Photothermal interferometer for gas-phase ammonia detection," *Anal. Chem.* **71**(7), 1391–1399 (1999).
8. L. Nicolaides and A. Mandelis, "Image-enhanced thermal-wave slice diffraction tomography with numerically simulated reconstructions," *Inverse Probl.* **13**(5), 1393–1412 (1997).
9. C. Zhou et al., "Photothermal optical coherence tomography in ex vivo human breast tissues using gold nanoshells," *Opt. Lett.* **35**(5), 700–702 (2010).
10. A. Gaiduk et al., "Room-temperature detection of a single molecule's absorption by photothermal contrast," *Science* **330**(6002), 353–356 (2010).
11. G. Busse, D. Wu, and W. Karpen, "Thermal wave imaging with phase sensitive modulated thermography," *J. Appl. Phys.* **71**(8), 3962–3965 (1992).
12. G. Busse, "From photothermal radiometry to lock-in thermography methods," *J. Phys. Conf. Ser.* **214**(1), 012003 (2010).
13. A. Hellen et al., "Optothermophysical properties of demineralized human dental enamel determined using photothermally generated diffuse photon density and thermal-wave fields," *Appl. Opt.* **49**(36), 6938–6951 (2010).
14. A. Mandelis, J. Batista, and D. Shaughnessy, "Infrared photocarrier radiometry of semiconductors: physical principles, quantitative depth profilometry, and scanning imaging of deep subsurface electronic defects," *Phys. Rev. B* **67**(20), 205208 (2003).
15. T. Wang et al., "Comparison of pulsed photothermal radiometry, optical coherence tomography and ultrasound for melanoma thickness measurement in PDMS tissue phantoms," *J. Biophoton.* **4**(5), 335–344 (2010).
16. I. A. Vitkin, B. C. Wilson, and R. R. Anderson, "Analysis of layered scattering materials by pulsed photothermal radiometry: application to photon propagation in tissue," *Appl. Opt.* **34**(16), 2973–2982 (1995).
17. A. Mandelis and C. Feng, "Frequency-domain theory of laser infrared photothermal radiometric detection of thermal waves generated by diffuse-photon-density wave fields in turbid media," *Phys. Rev. E* **65**(2), 021909 (2002).
18. N. Tabatabaei, A. Mandelis, and B. T. Amaechi, "Thermophotonic lock-in imaging of early demineralized and carious lesions in human teeth," *J. Biomed. Opt.* **16**(7), 071402 (2011).
19. J.-W. Kim et al., "Golden carbon nanotubes as multimodal photoacoustic and photothermal high-contrast molecular agents," *Nat. Nanotech.* **4**, 688–694 (2009).
20. D. Lasne et al., "Single nanoparticle photothermal tracking (SNaPT) of 5-nm gold beads in live cells," *Biophys. J.* **91**(12), 4598–4604 (2006).
21. V. P. Zharov, V. Galitovsky, and P. Chowdhury, "Nanocluster model of photothermal assay: application for high-sensitive monitoring of nicotine-induced changes in metabolism, apoptosis, and necrosis at a cellular level," *J. Biomed. Opt.* **10**(4), 044011 (2005).
22. V. P. Zharov et al., "In vivo photothermal flow cytometry: imaging and detection of individual cells in blood and lymph flow" *J. Cell. Biochem.* **97**(5), 916–932 (2006).
23. V. P. Zharov et al., "Integrated photothermal flow cytometry in vivo," *J. Biomed. Opt.* **10**(5), 051502 (2005).
24. E. I. Galanzha et al., "In vivo flow cytometry of circulating clots using negative photothermal and photoacoustic contrasts," *Cytom. Part A* **79A**(10), 814–824 (2011).
25. M. C. Skala et al., "Photothermal optical coherence tomography of epidermal growth factor receptor in live cells using immunotargeted gold nanospheres," *Nano Lett.* **8**(10), 3461–3467 (2008).
26. A. S. Paranjape et al., "Depth resolved photothermal OCT detection of macrophages in tissue using nanorose," *Biomed. Opt. Exp.* **1**(1), 2–16 (2010).
27. R. V. Kuranov et al., "Depth-resolved blood oxygen saturation measurement by dual-wavelength photothermal (DWP) optical coherence tomography," *Biomed. Opt. Exp.* **2**(3), 491–504 (2011).
28. R. V. Kuranov et al., "In vivo depth-resolved oxygen saturation by dual-wavelength photothermal (DWP) OCT," *Opt. Exp.* **19**(24), 23831–23844 (2011).
29. B. Li et al., "Performance evaluation of pulsed photothermal profiling of port wine stain in human skin," *Rev. Sci. Instrum.* **75**(6), 2048–2055 (2004).

30. D. McCormack et al., "Photoacoustic detection of melanoma micrometastasis in sentinel lymph nodes," *J. Biomech. Eng.* **131**(7), 074519 (2009).

31. H. Sontag and A. C. Tam, "Time-resolved flow-velocity and concentration measurements using a traveling thermal lens," *Opt. Lett.* **10**(9), 436–438 (1985).

32. A. Rose, R. Vyas, and R. Gupta, "Pulsed photothermal deflection spectroscopy in a flowing medium: a quantitative investigation," *Appl. Opt.* **25**(24), 4626–4643 (1986).

33. B. C. Li and R. Gupta, "Effect of optical saturation on pulsed photothermal deflection signals in flowing media," *J. Appl. Phys.* **88**(10), 5515–5526 (2000).

34. W. A. Weimer and N. J. Dovichi, "Time-resolved crossed-beam thermal lens measurement as a nonintrusive probe of flow velocity," *Appl. Opt.* **24**(18), 2981–2986 (1985).

35. K. Katayama, Y. Kikutani, and T. Kitamor, "Flow velocity detector in a microchip based on a photothermally induced grating," *Anal. Sci.* **23**(6), 639–643 (2007).

36. S. Ma, S. Yang, and D. Xing, "Photoacoustic imaging velocimetry for flow-field measurement," *Opt. Exp.* **18**(10), 9991–10000 (2010).

37. H. Fang, K. Maslov, and L. V. Wang, "Photoacoustic Doppler effect from flowing small light-absorbing particles," *Phys. Rev. Lett.* **99**(18), 184501 (2007).

38. H. Fang, K. Maslov, and L. V. Wang, "Photoacoustic Doppler flow measurement in optically scattering media," *Appl. Phys. Lett.* **91**(26), 264103 (2007).

39. J. Steketee, "Spectral emissivity of skin and pericardium," *Phys. Med. Biol.* **18**(5), 686–694 (1973).

40. A. Othonos and K. Kalli, *Fiber Bragg Gratings: Fundamentals and Applications in Telecommunications and Sensing*, Artech House Publishers, Norwood (1999).

41. R. Kashyap, *Fiber Bragg Gratings*, Academic Press, London (1999).

42. R. S. Quimby and A. I. Sheinis, "Photoacoustic effect in a flowing liquid," *Appl. Opt.* **26**(2), 363–371 (1987).

43. B. Monson, R. Vyas, and R. Gupta, "Pulsed and cw photothermal phase shift spectroscopy in a fluid medium: theory," *Appl. Opt.* **28**(13), 2554–2561 (1989).

44. K. Sreekumar and V. K. Vaidyan, "Measurement of thermal effusivity of liquids using a photothermal imager," *Meas. Sci. Technol.* **17**(4), 666–669 (2006).

45. S. Kaiplavil and A. Mandelis, "Highly depth-resolved chirped pulse photothermal radar for bone diagnostics," *Rev. Sci. Instrum.* **82**(7), 074906 (2011).

46. M. Xu and L. V. Wang, "Photoacoustic imaging in biomedicine," *Rev. Sci. Instrum.* **77**(4), 041101 (2006).

47. W. Zheng et al., "Optimal excitation-emission wavelengths for autofluorescence diagnosis of bladder tumors," *Int. J. Cancer* **104**(4), 477–481 (2003).

48. W. B. Jackson et al., "Photothermal deflection spectroscopy and detection," *Appl. Opt.* **20**(8), 1333–1344 (1981).

49. J. P. Woodcock, "Physical properties of blood and their influence on blood-flow measurement," *Rep. Prog. Phys.* **39**(1), 65–127 (1976).

50. J. C. Roark and R. A. Palmer, "Quantitative absorption spectra via photoacoustic phase angle spectroscopy," *Chem. Phys. Lett.* **60**(1), 112–116 (1978).

51. B. C. Li and R. Gupta, "Simultaneous measurement of absorption coefficient, thermal diffusivity, and flow velocity in a gas jet with pulsed photothermal deflection spectroscopy," *J. Appl. Phys.* **89**(2), 859–868 (2001).

52. P. Poulet, J. Chambron, and R. Unterreiner, "Quantitative photoacoustic spectroscopy applied to thermally thick samples," *J. Appl. Phys.* **51**(3), 1738–1742 (1980).

53. J. Bernal-Alvarado et al., "Mismatched mode thermal lens for assessing thermal diffusivity of serum and plasma from human blood," *Instrum. Sci. Technol.* **34**(1), 99–105 (2006).

54. H. Straube and O. Breitenstein, "Estimation of heat loss in thermal wave experiments," *J. Appl. Phys.* **109**(6), 064515 (2011).

55. R. Hoffman et al., *Hematology: Basic Principles and Practice*, Elsevier Churchill Livingstone, Philadelphia (2008).

56. R. A. McPherson, M. R. Pincus, and J. B. Henry, *Henry's Clinical Diagnosis and Management by Laboratory Methods*, Saunders Elsevier, Philadelphia (2006).

57. N. Katzilakis et al., "Spectral characteristics of acute lymphoblastic leukemia in childhood," *Leuk. Res.* **28**(11), 1159–1164 (2004).

58. E. L. Kaijzel et al., "Multimodal imaging and treatment of bone metastasis," *Clin. Exp. Metastasis* **26**(4), 371–379 (2009).

59. M. Nahavandi et al., "Near-infrared spectra absorbance of blood from sickle cell patients and normal individuals," *Hematology* **14**(1), 46–48 (2009).

60. T. Binzoni et al., "Blood volume and hemoglobin oxygen content changes in human bone marrow during orthostatic stress," *J. Physiol. Anthropol.* **25**(1), 1–6 (2006).

61. G. Uribe-Botero, J. G. Prichard, and H. J. Kaplowitz, "Bone marrow in HIV infection. A comparison of fluorescent staining and cultures in the detection of mycobacteria," *Am. J. Clin. Pathol.* **91**(3), 313–315 (1989).

62. A. F. Zuluaga et al., "Fluorescence excitation emission matrices of human tissue: a system for in vivo measurement and method of data analysis," *Appl. Spectrosc.* **53**(3), 302–311 (1999).

63. L. C. Aamodt and J. C. Murphy, "Effect of 3-D heat flow near edges in photothermal measurements," *Appl. Opt.* **21**(1), 111–115 (1982).

64. L. E. Kinsler and A. R. Frey, *Fundamentals of Acoustics*, p. 238, John Wiley, New York (1950).

65. H. Bach and N. Neuroth, *The Properties of Optical Glass*, Springer-Verlag, Heidelberg (1995).